



Efficient photocatalytic ozonation of azithromycin by three-dimensional g-C₃N₄ nanosheet loaded magnetic Fe-MCM-48 under simulated solar light

Yu Ling^{a,b}, Hai Liu^a, Binqing Li^c, Biaojun Zhang^b, Yixiao Wu^b, Heping Hu^d, Deyou Yu^e, Shaobin Huang^{b,*}

^a Jinan University, Guangzhou 510006, PR China

^b School of Environment and Energy, South China University of Technology, Higher Education Mega Center, Guangzhou 510006, PR China

^c Guangzhou Sewage Purification Co. Ltd., Guangzhou 510655, PR China

^d China Water Resources Pearl River Planning Surveying & Designing Co. Ltd., Guangzhou 510610, PR China

^e Engineering Research Center for Eco-Dyeing and Finishing of Textiles, Ministry of Education, Zhejiang Sci-Tech University, Hangzhou 310018, PR China



ARTICLE INFO

Keywords:

G-C₃N₄/Fe-MCM-48
Photocatalytic ozonation
Synergistic effect
Azithromycin

ABSTRACT

Magnetic g-C₃N₄/Fe-MCM-48 with unique 3-D structure was facilely prepared. MCM-48 framework was uniformly doped with Fe atoms, and then wrapped by g-C₃N₄ nanosheet to obtain ordered g-C₃N₄/Fe-MCM-48, which triggered an excellent synergistic effect and showed perfect activity and stability in photocatalytic ozonation of azithromycin (AZY). The removal rate of AZY by simulated solar light/g-C₃N₄/Fe-MCM-48/O₃ was close to 100% within 11 min, and the kinetic constant of catalysis with g-C₃N₄/Fe-MCM-48 was 9.2 times as much as that of g-C₃N₄ in coupling system. The synergy index was 8.6 for simulated solar light/g-C₃N₄/Fe-MCM-48/O₃. The influence of Fe contents and initial pH in the removal of AZY was investigated. The recycling of catalyst was significantly enhanced by excellent stability and magnetic property. Besides, the quenching experiments demonstrated that both hydroxyl radical and holes contributed to AZY removal, the possible removal pathway of photocatalytic ozonation of AZY had also been comprehensively studied.

1. Introduction

The pharmaceuticals and personal care products (PPCPs) would generate ecological safety and human health problems even if the concentration range from ng L⁻¹ to μ g L⁻¹, which had aroused increasing serious scientific and public concern as newly recognized environmental pollutants in recent decades [1,2]. As a widely used antibiotic, azithromycin (AZY) was difficult to be degraded than other macrolides, and some wastewater treatment plants in China reported AZY with the lowest removal efficiency (6.3%) among the common antibiotics in wastewaters [3,4]. In addition, in the process of pharmaceutical wastewater treatment, the concentration of AZY easily reached mg L⁻¹ level. Advanced oxidation processes (AOPs) was characterized by the production of hydroxyl radical (•OH) with strong oxidation ability. Under the reaction conditions of high temperature and high pressure, electric, ultrasonic, light irradiation and catalyst, the refractory macromolecular organics was degraded into non-toxic CO₂ and H₂O [5–7]. According to the way of generating free radicals and the different

reaction conditions, they were divided into photocatalysis [8], ozonation [9], Fenton oxidation [10], peroxymonosulfate oxidation [11], electrochemical oxidation [12], and sonochemical oxidation [13]. However, coupling AOPs with other chemicals or technologies were being spent on to improve its capability, such as O₃/Fe/ultrasound [14], ozonation/peroxymonosulfate oxidation [15], O₃/H₂O₂ [16] and UV/TiO₂/O₃ [17].

Photocatalytic ozonation as an emerging AOP which showed high removal efficiency for refractory pollutants. A large number of reactive oxygen species (ROSSs, i.e. •OH, holes (h⁺), •O₃[•], •O₂[•], surface O) were produced by synergistic effect between photocatalysis and ozonation. The production of bromate and other harmful substances was effectively inhibited in the process of photocatalytic ozonation [18–20]. Many photocatalytic ozonation studies mainly focused on the modification of TiO₂, but the further application of TiO₂ was limited by the fact that it only responded to ultraviolet (a small portion of sunlight) [21–24]. g-C₃N₄ as a metal-free organic polymer and visible-driven semiconductor photocatalyst, had attracted extensive attention due to its

* Corresponding author.

E-mail addresses: 245401495@qq.com (Y. Ling), liuhai@jnu.edu.cn (H. Liu), libiqing@sohu.com (B. Li), zbj19930422@163.com (B. Zhang), wuyixiao77@126.com (Y. Wu), hhp023@163.com (H. Hu), yudeyou92@zstu.edu.cn (D. Yu), chshuang@scut.edu.cn (S. Huang).

advantages of non-toxic, cheap, high visible light absorption capacity, suitable band gap and high physics-chemistry stability [25]. Recently, the modification methods mainly focused on noble metal doping, non-metal doping and synthesis heterojunction to overcome the defects of high photo-induced carriers recombination rate and low visible light utilization rate of g-C₃N₄ [26,27]. However, many studies focused on the photocatalysis efficiency of catalysts in photocatalytic ozonation of refractory pollutant, the improvement of ozonation efficiency was ignored.

It was well known that increased the specific surface area of g-C₃N₄ and introduced Fe could significantly improve the catalytic activity of photocatalysis and ozonation, respectively [28–30]. The mesoporous molecular sieves were used as excellent template of g-C₃N₄ because of superior physics-chemistry stability and high specific surface area. Compared with other mesoporous molecular sieves, the MCM-48 had highly interwoven and branched structures that would overcome pore blocking and collapse in the process of Fe doping, two independent three-dimensional pore systems of MCM-48 provided a good mass transfer efficiency for photocatalytic ozonation [31,32]. Furthermore, plentiful Lewis acid sites were produced when metal oxides appeared on the surface of MCM-48, but the loaded metals were easily dissolved into the water during catalytic reaction [33]. In this study, Fe-MCM-48 was synthesized by doping cheap Fe atoms into the framework of MCM-48, three-dimensional g-C₃N₄/Fe-MCM-48 was obtained by wrapping g-C₃N₄ nanosheet on the surface of Fe-MCM-48. The g-C₃N₄/Fe-MCM-48 not only owned unique and stable microstructure for promoting the production of ROSs, but also owned excellent magnetic characteristic for facilitating the recycling of catalyst. As a novel environment function material, the physics-chemistry properties of g-C₃N₄/Fe-MCM-48 were well studied and presented in this work. Meanwhile, the detailed AZY removal efficiency, pathways and mechanisms in simulated solar light/g-C₃N₄/Fe-MCM-48/O₃ (SSL/g-C₃N₄/Fe-MCM-48/O₃) were investigated.

2. Experimental

2.1. Reagents and materials

AZY with purity > 99%, cetyltrimethylammonium bromide (CTAB, analytical grade), tetraethyl orthosilicate (TEOS, analytical grade), iron (III) nitrate nonahydrate (Fe(NO₃)₃·9 H₂O, analytical grade), dicyandiamide (C₂H₄N₈, >99%) were supplied by Shanghai Macklin Biochemical Co. Ltd, (China). Other reagents were purchased from Tianjin Kermel Chemical Reagents Ltd. and used without purification. All solutions used in this work were prepared by deionized water.

2.2. Catalysts preparation

MCM-48 was obtained via a hydrothermal method reported elsewhere [34]. Fe doped MCM-48 framework was obtained by the facile one-pot method. In brief, a certain amount of CTAB as template agent was added into alkaline solution (NaOH, 0.75 M, 70 mL) at 313 K to yield a homogenous mixture, 15 mL TEOS as silica source was added into above solution and stirring vigorously for 2 h. Afterwards, 5 mL different concentration of iron nitrate solution as active species to form the unique Si-O-Fe was added into mixture and stirred constantly for 6 h. The above mixture was transferred into a Teflon-lined autoclave at 373 K for 72 h. The resulting product was filtered off, washed, and dried at 333 K for 24 h. The X% Fe-MCM-48 was obtained with a Fe(NO₃)₃·9 H₂O/CTAB mass ratio of X% after calcined in air at 823 K for 6 h. The pure MCM-48 was obtained in the same way without addition of Fe (NO₃)₃·9 H₂O.

1 g of dicyandiamide dissolved in 30 mL deionized water was mixed with 0.5 g X% Fe-MCM-48 and stirred at 313 K for 3 h, then the above mixture was heated at 353 K until the water was removed. Finally, the resultant solid was calcined at 823 K for 2 h in air. The g-C₃N₄/X% Fe-

MCM-48 was successfully obtained.

2.3. Characterizations

The crystalline phase of the samples was determined on X-ray diffraction (XRD, BRUKER D8 ADVANCE) using Cu K α radiation. The specific surface area of the samples was calculated on Brunauer-Emmett-Teller analysis (BET, ASAP 2020, Micromeritics, America) using nitrogen adsorption-desorption isotherms at 77 K. The morphology of the sample was observed on scanning electron microscopy (SEM, JSM-6510, JEOL, Japan). The structure and EDX elemental mapping images of the sample were studied on transmission electron microscopy (TEM, JEM-2100HR, JEOL, Japan). Fourier transform infrared (FTIR) spectra were recorded on a Nicolet 6700 spectrophotometer with KBr as the reference sample. X-ray photoelectron spectra (XPS) were examined on a multi-functional imaging electron spectrometer (Thermo ESCALAB 250XI, America). The optical absorption properties of the samples were measured on UV-Vis spectrophotometer (U-3010, HITACHI, Japan) with BaSO₄ reference. The magnetic property (M-H curve) of the sample was measured at 300 K on a vibrating sample magnetometer (MPMS-XL-7, Quantum Design). Photoluminescence (PL) spectra were analyzed on the Shimadzu RF-6000 Spectro fluorophotometer. Electrochemical impedance spectroscopy (EIS) experiment was carried out on electrochemical workstation (Shanghai, China). Solid electron paramagnetic resonance (EPR) spectroscopy was conducted on the Bruker model A 300 spectrometer equipped with a 300 W Xe-lamp at 100 K. The microwave frequency was set as 10.1 GHz, the microwave power was 19.1 dB, and the tested samples were quantitative weighted with 50 mg. Electron spin resonance (ESR) signal of hydroxyl radicals (·OH) was examined by the probe molecule DMPO at room temperature, with the light source being a 300 W Xe-lamp.

2.4. Photocatalytic ozonation experiments

The structure of reactor (Fig. S1) was described in detail. Photocatalytic ozonation experiments were conducted in a 1 L glass tubular photoreactor (h = 400 mm, Φ_{in} = 85 mm), equipped with a cylindrical high pressure xenon long-arc lamp (h = 250 mm, Φ = 25 mm, GXH500W, Beijing NBET Technology Co., Ltd) as the SSL irradiation source. The lamp was placed inside a double-deck quartz water-cooling thimble (h = 350 mm, Φ_{in} = 30 mm, Φ_{out} = 55 mm) to maintain the temperature at 298 K. The illumination intensity of Xenon lamp was 48 mW cm⁻² (Measured by Radiometers of model FZ-A, Photoelectric Instrument Factory Beijing Normal University). About 0.2 g catalyst was added to 1 L AZY solution with a concentration of 50 mg L⁻¹. O₃ was generated from ozone generator (ANSEROS, COM-AD-01-OEM) and the flow rate was maintained at 1 L min⁻¹. The yield of O₃ was 50 mg h⁻¹. It was continuously bubbled into the solution through a porous glass plate which was immobilized at the bottom of reactor. At the beginning of reaction, the suspension was firstly bubbled with O₂ for 30 min to establish adsorption/desorption equilibrium. Samples were withdrawn at specific time intervals and filtered using syringe filters (pore size: 0.45 μ m). The filtrate was collected and analyzed further. As a quencher, Na₂S₂O₃ solution was added into the filtrate to avoid the continuous oxidation.

2.5. Analytical procedures

The concentration of AZY was measured on high performance liquid chromatography (Shimadzu, LC10A HPLC) equipped with a UV detector (SPD-10AV) at 274 nm and a Eclipse XDBC18 (4.6 \times 150 mm, 5 μ m) reverse phase column. The mobile phase was composed of 50% A (0.1% HCOOH in water) and 50% B (0.1% HCOOH in acetonitrile) (0.8 mL min⁻¹ flow rate). The intermediates in AZY removal were detected on HPLC-MS/MS (Thermo Scientific Ultimate 3000 RSLC and Q Exactive Orbitrap) with an electrospray ionization (ESI) source. The packed HPLC

column was used (Shim-pack VP-ODS 250 L \times 2.0 and P/N 228–34937–95, Shimadzu) at a column temperature of 313 K, while the relevant requirements were the same as the above-mentioned chromatographic condition of HPLC.

3. Results and discussion

3.1. Characteristics of catalysts

Fig. 1a showed the wide angle XRD patterns of samples. Extended diffraction peaks near 15–25° in g-C₃N₄/Fe-MCM-48 and Fe-MCM-48 relate to amorphous SiO₂ [35]. The absence of characteristic peaks of Fe_xO_y meant that the Fe atoms were uniformly doped into MCM-48 framework. The weak diffraction peak at $2\theta = 27.3$ corresponded to (002) plane of g-C₃N₄, which indicated the highly dispersed g-C₃N₄ nanosheet on the surface of g-C₃N₄/Fe-MCM-48. The results expressed that the ordered mesoporous structure of MCM-48 could be maintained with doping Fe atoms and loading g-C₃N₄ nanosheet in g-C₃N₄/Fe-MCM-48.

Fig. 1b–c showed the N₂ adsorption-desorption isotherms and pore size distribution curves of samples. As showed in Fig. 1b, all the samples exhibited a type IV isotherm and one hysteresis loop, which was a vital characteristic of mesoporous materials. As showed in Fig. 1c, Fe-MCM-48 maintained the unique channel structure of MCM-48, and mesoporous structure could be observed from g-C₃N₄/Fe-MCM-48. Their pore structure parameters were listed in Table 1. According to the results, the specific surface area of Fe-MCM-48 was 659 m² g⁻¹, which indicated the partial replacement of Si by Fe in the framework of MCM-48 might inevitably cause slight reduction of the surface area. Compared with

Table 1
Pore structure parameters of the samples.

Samples	BET (m ² g ⁻¹)	V _p (cm ³ g ⁻¹)	D _p (nm)
5% Fe-MCM-48	659	0.61	2.7
g-C ₃ N ₄ /5% Fe-MCM-48	165	0.35	1.5–8
g-C ₃ N ₄	5.3	–	–

bulk g-C₃N₄, the specific surface area of g-C₃N₄/Fe-MCM-48 increased by 31 times to 165 m² g⁻¹, it still had satisfactory pore diameter (1.5–8 nm) and pore volume (0.35 cm³ g⁻¹) after coated by g-C₃N₄ nanosheet.

Fig. 2(a–b) displayed the TEM images of g-C₃N₄/Fe-MCM-48. The g-C₃N₄/Fe-MCM-48 exhibited regularly spherical morphology (with a controllable diameter of approximately 500 nm) similar to MCM-48. Compared with MCM-48 (with a pore size of approximately 3.2 nm), the pore size of g-C₃N₄/Fe-MCM-48 (about 2.3 nm) decreased slightly due to wrapped by g-C₃N₄ nanosheet, while it sustained a long-range ordered cubic pore structure. Fig. 2c displayed the electron diffraction image of g-C₃N₄/Fe-MCM-48. No crystalline Fe compounds were observed from the electron diffraction pattern, which suggested that Fe exists mainly in the form of Si-O-Fe. Fig. 2d displayed the EDS spectrum of g-C₃N₄/Fe-MCM-48. It revealed that Fe, Si, O, C and N elements were present, which were consistent with XRD characterization.

Fig. 3 depicted FTIR spectra of samples. It could be seen that g-C₃N₄/Fe-MCM-48 had both the characteristic absorption bands of g-C₃N₄ and Fe-MCM-48. In the characteristic absorption bands of g-C₃N₄, the peak observed at 800 cm⁻¹ was assigned to the characteristic breathing of the tri-s-triazine units, other peaks located at 1240, 1320, 1410, 1570 and

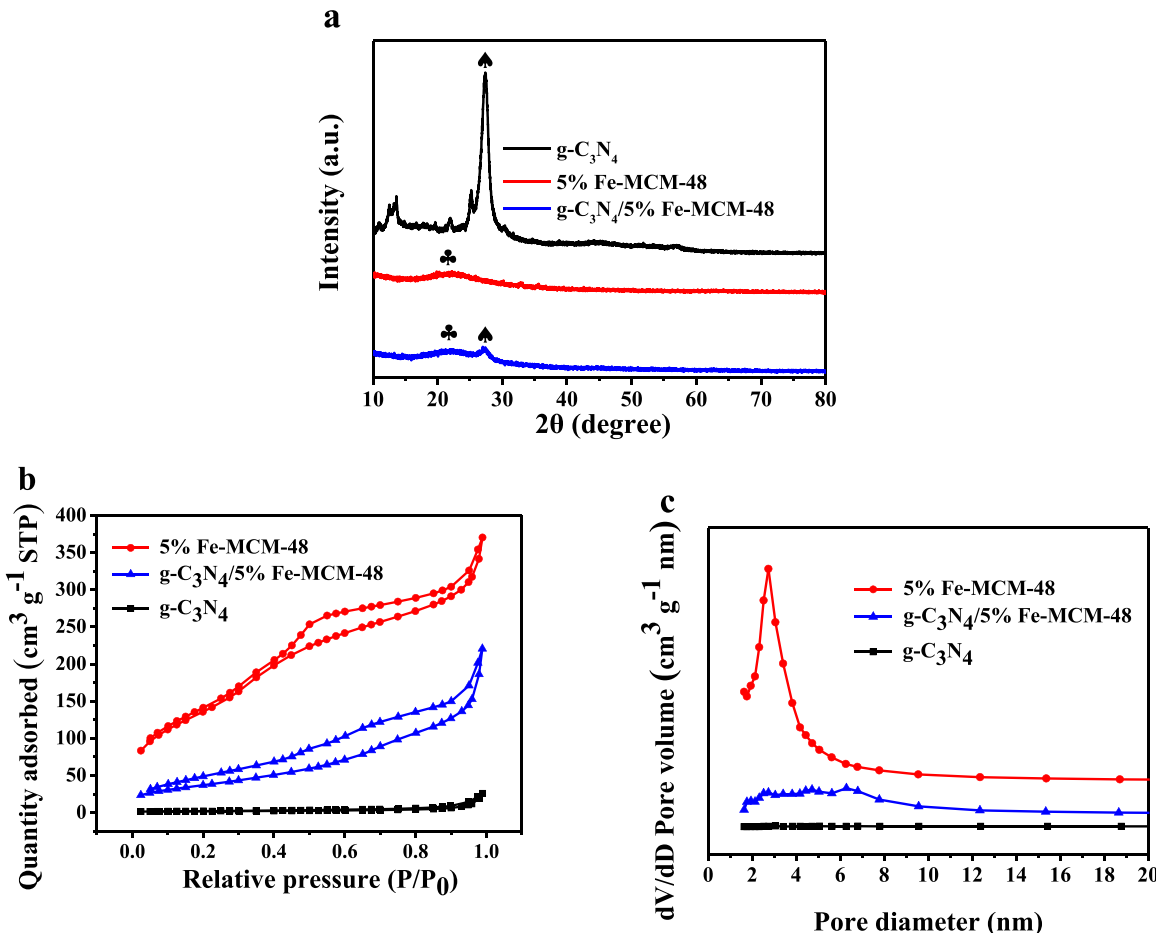


Fig. 1. XRD pattern (a), N₂ adsorption-desorption isotherms (b) and pore size distribution (c) of samples.

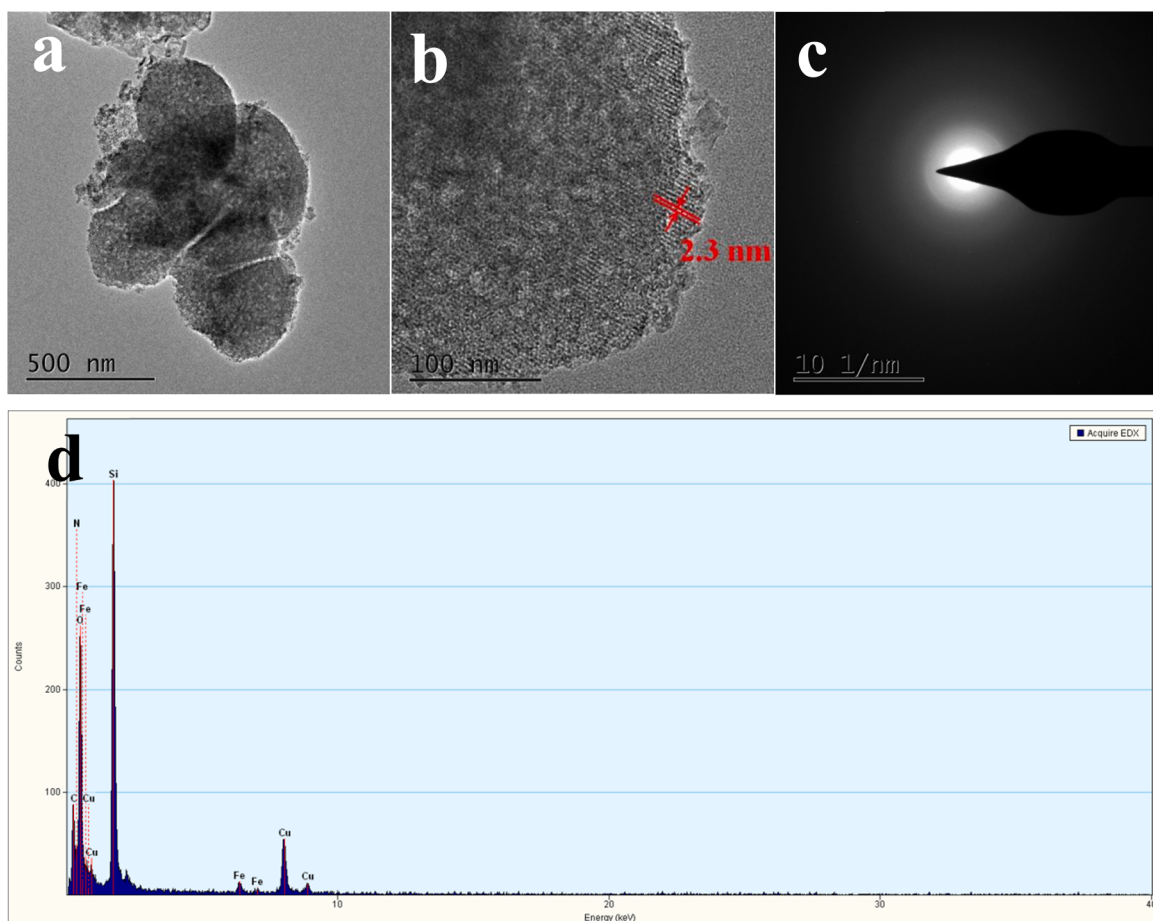


Fig. 2. . TEM images (a-b), electron diffraction (c) and EDS spectrum (d) of g-C₃N₄/5% Fe-MCM-48.

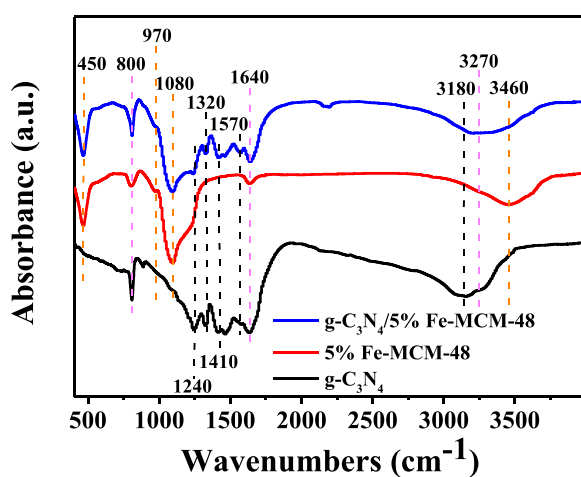


Fig. 3. FTIR spectra of samples.

1640 cm⁻¹ corresponded to the stretching and rotation vibration of the C-N and C≡N bonds in the g-C₃N₄ nanosheet [36,37]. Insignificant difference was found between the characteristic absorption bands of Fe-MCM-48 and pure MCM-48, suggesting that Fe-doping exhibited limited influence on chemical bonds of MCM-48. The peaks observed at 450, 800 and 1080 cm⁻¹ were related to the bending vibration, stretching vibration and antisymmetric stretching vibration of Si-O-Si, respectively [38]. The peaks located at 970 cm⁻¹ and 1640 cm⁻¹ were attributed to the stretching vibration of Si-OH and the bending vibration

of SiO-H, respectively [39,40]. Besides, the broad peak of g-C₃N₄/Fe-MCM-48 at 3270 cm⁻¹ not only represented the stretching mode of N-H bond in g-C₃N₄ nanosheet (at 3460 cm⁻¹), but also represented the characteristic O-H stretching of hydrogen bonded surface silanol groups in the Fe-MCM-48 matrix (at 3180 cm⁻¹). Strong interaction between species inside and outside the g-C₃N₄/Fe-MCM-48 structure was vital to realize multifunctional processes in photocatalytic ozonation of organic pollutants.

Fig. 4 showed XPS spectrum of g-C₃N₄/Fe-MCM-48. XPS was employed to analyze the chemical states of five elements in g-C₃N₄/Fe-MCM-48. The wide scan spectrum indicated the presence of C, N, O, Si and Fe elements in g-C₃N₄/Fe-MCM-48 (Fig. 4a). Fig. 4b showed the high-resolution C 1 s spectra, exhibiting two characteristic peaks at 285 and 288 eV, which were ascribed to the C-C bond and the sp²-hybridized carbon of N-C≡N coordination [41,42]. The N 1 s spectrum (Fig. 4c) included three peaks at 398.7, 400.2 and 401 eV, which were attributed to the sp²-hybridized aromatic nitrogen bonding to carbon atoms (C=N=C), the tertiary nitrogen (N-(C)₃) and the free amino groups (C-N-H), respectively [43]. The O 1 s spectrum of catalyst was displayed in Fig. 4d, in which the peak at 533.5 eV was assigned to the Si-O-Fe. The presence of lattice oxygen but no adsorbed oxygen indicated that the catalyst did not form Fe_xO_y. The replacement of silanol groups by Fe species could be further proved in Fig. 4e. The peak of Si 2p was shifted to 104.3 eV indicated the massive Si-O-Fe mixed-bond formation in the catalyst framework [44]. The spectrum of Fe 2p for g-C₃N₄/Fe-MCM-48 showed two main peaks (with $\Delta = 13.6$ eV) at approximately 713.9 and 727.5 eV (Fig. 4f), which were assigned to Fe 2p_{3/2} and Fe 2p_{1/2} of Fe³⁺, respectively [45]. Compared with Fe₂O₃ (710.7 and 724.3 eV for 2p_{3/2} and 2p_{1/2}, respectively), the signals for Fe 2p obviously shifted to higher binding energies, indicating that Fe³⁺ was not existing as oxide but

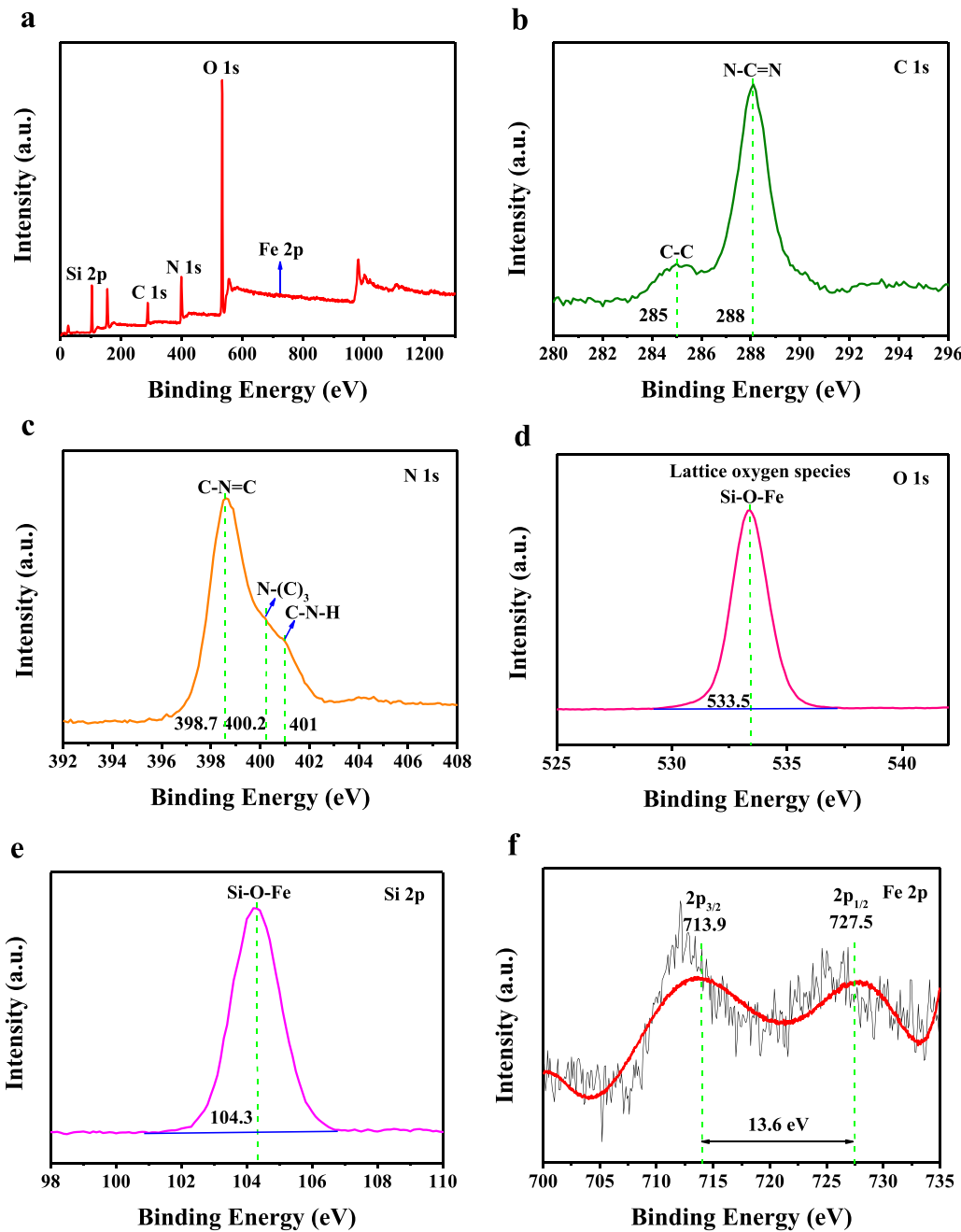


Fig. 4. XPS spectra of wide scan (a), C 1 s (b), N 1 s (c), O 1 s (d), Si 2p (e) and Fe 2p (f) of g-C₃N₄/5% Fe-MCM-48.

replaced Si⁴⁺ to generate Si-O-Fe bond [46].

Fig. 5a displayed UV-vis DRS spectra of samples. The g-C₃N₄/Fe-MCM-48 exhibited a strong absorption in the visible region, where it appeared a remarkable red shift compared to g-C₃N₄. The introduction of MCM-48 gave g-C₃N₄/Fe-MCM-48 larger light radiation area, which was a momentous reason for the increase of light absorption intensity. The absorption edge of g-C₃N₄/Fe-MCM-48 was about 545 nm (g-C₃N₄ was about 457 nm), which implied its narrower band gap than g-C₃N₄. According to the Kubelka-Munk function ($\alpha h\nu = A(h\nu - E_g)^n$), the estimated band gap (E_g) values for g-C₃N₄ and g-C₃N₄/Fe-MCM-48 were 2.71 eV and 2.27 eV, respectively. The band structure of Fe modified g-C₃N₄ had been discussed previously [47,48]. Band gap played an important role in the photocatalytic performance of semiconductor materials and further affected the synergistic effect of photocatalytic ozonation. Therefore, the excellent optical properties of g-C₃N₄/Fe-MCM-48 would significantly improve the yield of ROSSs.

Fig. 5b displayed PL spectra of samples. It was well acknowledged that the utilization of photo-induced carriers was closely related to photocatalytic efficiency. The migration, transfer, and recombination of photo-induced carriers were studied by PL, and lower PL intensity denoted lower recombination rate of photo-induced carriers. PL intensity was found to follow the sequence: g-C₃N₄ > g-C₃N₄ + O₃ > g-C₃N₄/Fe-MCM-48 > g-C₃N₄/Fe-MCM-48 + O₃. All processes exhibited a strong PL emission peak at around 440 nm, but the characteristic peak intensity of pure g-C₃N₄ was much higher than that of g-C₃N₄/Fe-MCM-48. It was because the increase in specific surface area promoted the transfer of photo-induced electrons and holes, and the highly dispersed Fe atoms helped electrons to be emitted outwards. The decrease of PL intensity due to the presence of O₃ was mainly attributed to the synergistic effect between photocatalysis and ozonation (O₃ as a good electron acceptor). The lowest PL intensity was seen for g-C₃N₄/Fe-MCM-48 in coupled system, pointing out the minimum photo-induced carriers

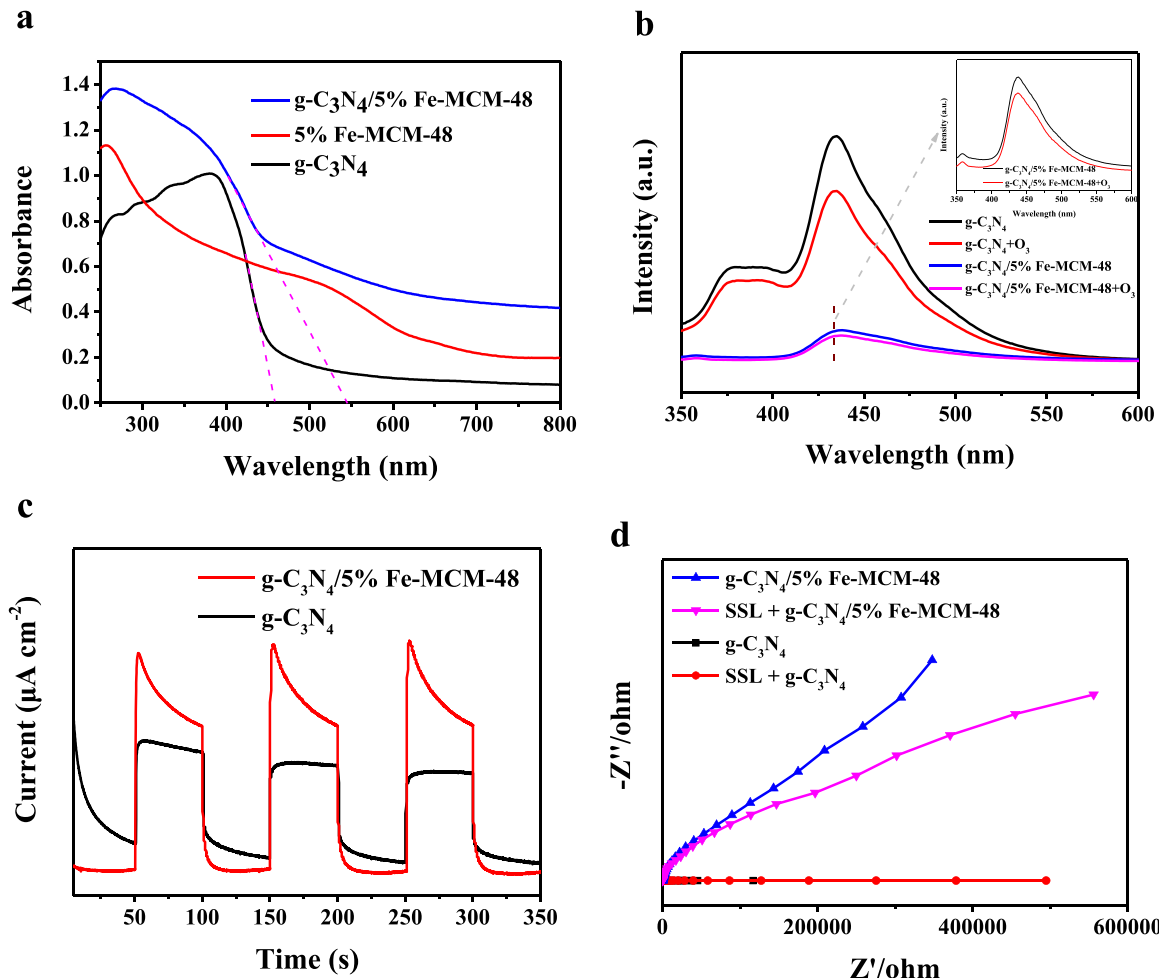


Fig. 5. UV-vis DRS spectra (a), PL spectra (b), transient photocurrent responses (c) and EIS Nyquist plots (d) of samples.

recombination rate against AZY.

Fig. 5c displayed transient photocurrent responses of $\text{g-C}_3\text{N}_4$ and $\text{g-C}_3\text{N}_4/\text{Fe-MCM-48}$. It was well known that the higher photocurrent response corresponded to the more photo-induced electrons. The photocurrent response of $\text{g-C}_3\text{N}_4/\text{Fe-MCM-48}$ was stronger, which further proved that catalyst facilitated electrons transfer on the surface and inhibited photo-induced carriers recombination. Reproducible ON/OFF illumination cycles proved the stable photoelectrochemistry properties of $\text{g-C}_3\text{N}_4/\text{Fe-MCM-48}$. As showed in Fig. 5d, the EIS Nyquist plots was used to evaluate the conductivity of samples. The smaller Nyquist plot radius meant the faster rate of the interface charge carriers transfer [49]. It could be found that the Nyquist plot radius of the $\text{g-C}_3\text{N}_4/\text{Fe-MCM-48}$ was much smaller than that of bulk $\text{g-C}_3\text{N}_4$, which implied both Fe doping and $\text{g-C}_3\text{N}_4$ nanosheet improved the conductivity of $\text{g-C}_3\text{N}_4/\text{Fe-MCM-48}$. The radius of the impedance ring obviously decreased after adding SSL.

3.2. The removal of AZY in different processes

The photocatalytic ozonation efficiency of $\text{g-C}_3\text{N}_4/\text{Fe-MCM-48}$ was investigated through the removal of AZY under SSL irradiation and low concentration O_3 . As showed in Fig. 6a, the AZY was stable under SSL/ $\text{g-C}_3\text{N}_4/\text{Fe-MCM-48}$ and $\text{O}_3/\text{g-C}_3\text{N}_4/\text{Fe-MCM-48}$ with 33.4% and 9.4% AZY removals. On the other hand, only less than 7% AZY removals was observed in SSL/ $\text{g-C}_3\text{N}_4$ and $\text{O}_3/\text{g-C}_3\text{N}_4$ within 11 min. Moreover, $\text{g-C}_3\text{N}_4/\text{Fe-MCM-48}$ exhibited the best catalytic activity and synergistic effect in the coupled system, and the removal rate of AZY was 98.8%, while $\text{g-C}_3\text{N}_4$ was only 37.3%. This improvement proved that the highly

dispersed Fe atoms not only greatly accelerated separation of photo-induced carriers but also acted as active centers for ozonation. The large specific surface area of $\text{g-C}_3\text{N}_4/\text{Fe-MCM-48}$ also provided abundant active sites for AZY removal.

As showed in Fig. 6b, AZY removal was well fitted by the pseudo first-order kinetics ($\ln(C_0/C_t) = kt$). The kinetic constant (k) increased in the order of $\text{O}_3/\text{g-C}_3\text{N}_4$ (0.003 min^{-1}) $<$ SSL/ $\text{g-C}_3\text{N}_4$ (0.004 min^{-1}) $<$ $\text{O}_3/\text{g-C}_3\text{N}_4/\text{Fe-MCM-48}$ (0.008 min^{-1}) $<$ SSL/ $\text{g-C}_3\text{N}_4/\text{Fe-MCM-48}$ (0.036 min^{-1}) $<$ SSL/ $\text{g-C}_3\text{N}_4/\text{O}_3$ (0.041 min^{-1}) $<$ SSL/ $\text{g-C}_3\text{N}_4/\text{MCM-48}/\text{O}_3$ (0.048 min^{-1}) $<$ SSL/ $\text{Fe-MCM-48}/\text{O}_3$ (0.126 min^{-1}) $<$ SSL/ $\text{g-C}_3\text{N}_4/\text{Fe-MCM-48}/\text{O}_3$ (0.378 min^{-1}). The kinetic constant of AZY with SSL/ $\text{g-C}_3\text{N}_4/\text{Fe-MCM-48}/\text{O}_3$ was 3.0 and 9.2 times as much as that of SSL/ $\text{Fe-MCM-48}/\text{O}_3$ and SSL/ $\text{g-C}_3\text{N}_4/\text{O}_3$, respectively. Furthermore, kinetic constant was used to calculate synergy index ($\eta = k_{\text{photocatalytic ozonation}}/(k_{\text{photocatalysis}} + k_{\text{ozonation}})$), the synergy index of photocatalytic ozonation of AZY by SSL/ $\text{g-C}_3\text{N}_4/\text{Fe-MCM-48}/\text{O}_3$ ($\eta = 8.6$) was higher than that of SSL/ $\text{g-C}_3\text{N}_4/\text{O}_3$ ($\eta = 5.9$). These results were consistent with the expected effect and further demonstrated the superiority of $\text{g-C}_3\text{N}_4/\text{Fe-MCM-48}$ in AOPs.

The catalyst activity also depended strongly on the rate of photon absorption in the reactor and this varied with catalyst concentration and with catalyst specimens. As showed in Fig. S2, the optical intensity distribution of xenon lamp could be obtained. The optical absorption intensity of catalysts with different concentration was showed in Fig. S3. The optical reflectance rate of solid catalysts was showed in Fig. S4. The related optical parameters could be calculated by Eqs. (1–6) [50–54]. The spectral-averaged specific absorption coefficient κ^* and specific scattering coefficients σ^* of $\text{g-C}_3\text{N}_4/\text{Fe-MCM-48}$ were calculated to be

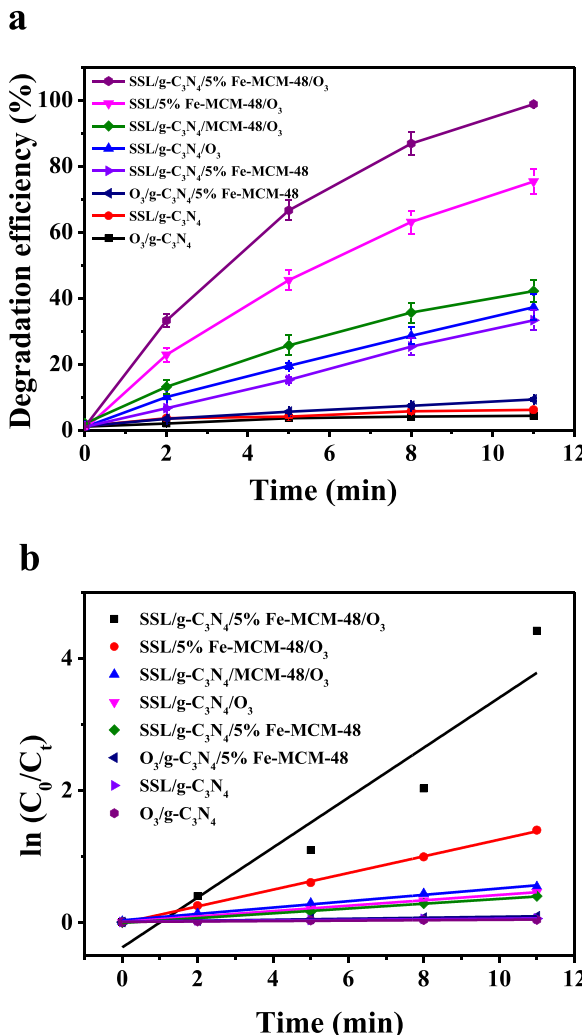


Fig. 6. AZY removal by different processes (a), pseudo first-order kinetics fitting for AZY removal within the reaction time of 11 min (b). Reaction conditions: O₃ dose = 50 mg h⁻¹, flow rate of oxygen = 1.0 L min⁻¹, catalyst dose = 0.2 g L⁻¹, initial concentration of AZY = 50 ppm, SSL intensity = 48 mW cm⁻², and temperature = 298 K.

1.78 and 0.12, while g-C₃N₄ were calculated to be 0.96 and 0.04. The optical absorption and scattering ability of g-C₃N₄/Fe-MCM-48 were significantly improved, which promoted the catalytic activity to a certain extent. In this reactor, the optical thickness τ of g-C₃N₄/Fe-MCM-48 and g-C₃N₄ were calculated to be 0.57 and 0.3, respectively. The reactor had excellent irradiation penetration effect on suspension and minimized the influence of thickness, which was widely used in the research of photocatalytic ozonation technology.

According to the optical thickness τ of g-C₃N₄/Fe-MCM-48 and g-C₃N₄. Equal optical thickness meant that the concentration of g-C₃N₄ was 1.9 times that of g-C₃N₄/Fe-MCM-48. The degradation effect of catalysts with equal optical thickness was showed in Fig. S5. Although the concentration of g-C₃N₄ was nearly doubled, the catalytic activity of it in the coupled system was much lower than that of g-C₃N₄/Fe-MCM-48.

$$\beta\lambda = \frac{2.303 ABS_{\lambda}}{L} \quad (1)$$

$$\kappa_{\lambda}^* = \kappa_{\lambda}^* + \sigma_{\lambda}^* \quad (2)$$

$$F(R) = \frac{(1-R)^2}{2R} = \frac{\kappa_{\lambda}^*}{\sigma_{\lambda}^*} \quad (3)$$

$$\kappa^* = \frac{\int_{\lambda_{\min}}^{\lambda_{\max}} \kappa_{\lambda}^* I_{\lambda} d\lambda}{\int_{\lambda_{\min}}^{\lambda_{\max}} I_{\lambda} d\lambda} \quad (4)$$

$$\sigma^* = \frac{\int_{\lambda_{\min}}^{\lambda_{\max}} \sigma_{\lambda}^* I_{\lambda} d\lambda}{\int_{\lambda_{\min}}^{\lambda_{\max}} I_{\lambda} d\lambda} \quad (5)$$

$$\tau = (K^* + \sigma^*) C_{\text{cat}} \delta \quad (6)$$

Symbols	Explanation
β_{λ}	extinction coefficients of catalyst aqueous suspensions
ABS _λ	absorbance
L	cell length
β_{λ}^*	specific extinction coefficient
κ_{λ}^*	specific absorption coefficient
σ_{λ}^*	specific scattering coefficient
R	infinite reflectance value of the catalyst solid
κ^*	spectral-averaged specific absorption coefficients
σ^*	spectral-averaged specific scattering coefficients
I_{λ}	spectrum of the incident irradiation
λ_{\min}	minimum wavelengths of the incident radiation
λ_{\max}	maximum wavelengths of the incident radiation
τ	optical thickness
C_{cat}	concentration of the catalyst
δ	characteristic length for the extinction of the light inside the reactor

3.3. Analysis of influencing factors and catalyst reuse

Fig. 7a showed the effect of pH on AZY removal by coupled system with g-C₃N₄/Fe-MCM-48. The effect of pH was an important factor in the photocatalytic ozonation of AZY because pH would transform removal pathways. The best AZY removal efficiency was achieved when the initial pH of AZY solution was adjusted to 9. The pK_a value for AZY was 8.7 and pH_{pzc} (point of zero charge) for g-C₃N₄/Fe-MCM-48 was found to be 9.2 [55]. The charge between the surface of catalyst and AZY was opposite when pH = 9, which increased the electrostatic interaction for better adsorption on to catalyst surface. On the contrary, the electrostatic repulsion worked at the pH < 8.7 or pH > 9.2, which could reduce the contact reaction between catalyst and AZY. The removal efficiency of AZY at alkaline pH was generally higher than that at acidic pH, one reason for this was that alkaline medium facilitated the conversion of O₃ into •OH. In addition, alkaline medium offered ample hydroxide ions that reacted with holes on the catalyst surface and generated •OH. The optical absorption intensity of g-C₃N₄/Fe-MCM-48 with different pH was showed in Fig. S6. The optical absorption intensity increases slightly with the increase of pH. The results showed that the effect of pH on optical thickness was important, which meant the increase of pH would promote the optical properties.

Fig. 7b showed the effect of Fe(NO₃)₃•9 H₂O/CTAB mass ratio on the photocatalytic ozonation of AZY. The catalytic activity of Fe-doped samples were significantly higher than that of g-C₃N₄/MCM-48, which indicated that Fe doping was vital for the improvement of photocatalytic ozonation efficiency. The g-C₃N₄/5% Fe-MCM-48 sample revealed the highest catalytic efficiency for photocatalytic ozonation of AZY. With Fe doping in MCM-48, AZY removal efficiency was enhanced due to the presence of active sites. Fe atoms on g-C₃N₄ nanosheet was favorable for photo-induced electrons transfer and O₃ decomposition. However, the removal of AZY was inhibited when the mass ratio of Fe(NO₃)₃•9 H₂O/CTAB exceeds 5%. Due to the channel of MCM-48 might be blocked by superfluous Fe and thereby reduced the mass transfer efficiency. The excessive amount of Fe might made Fe atoms as the recombination centers of photo-induced carriers. The superfluous Fe would also inhibit the optical absorption properties of catalyst.

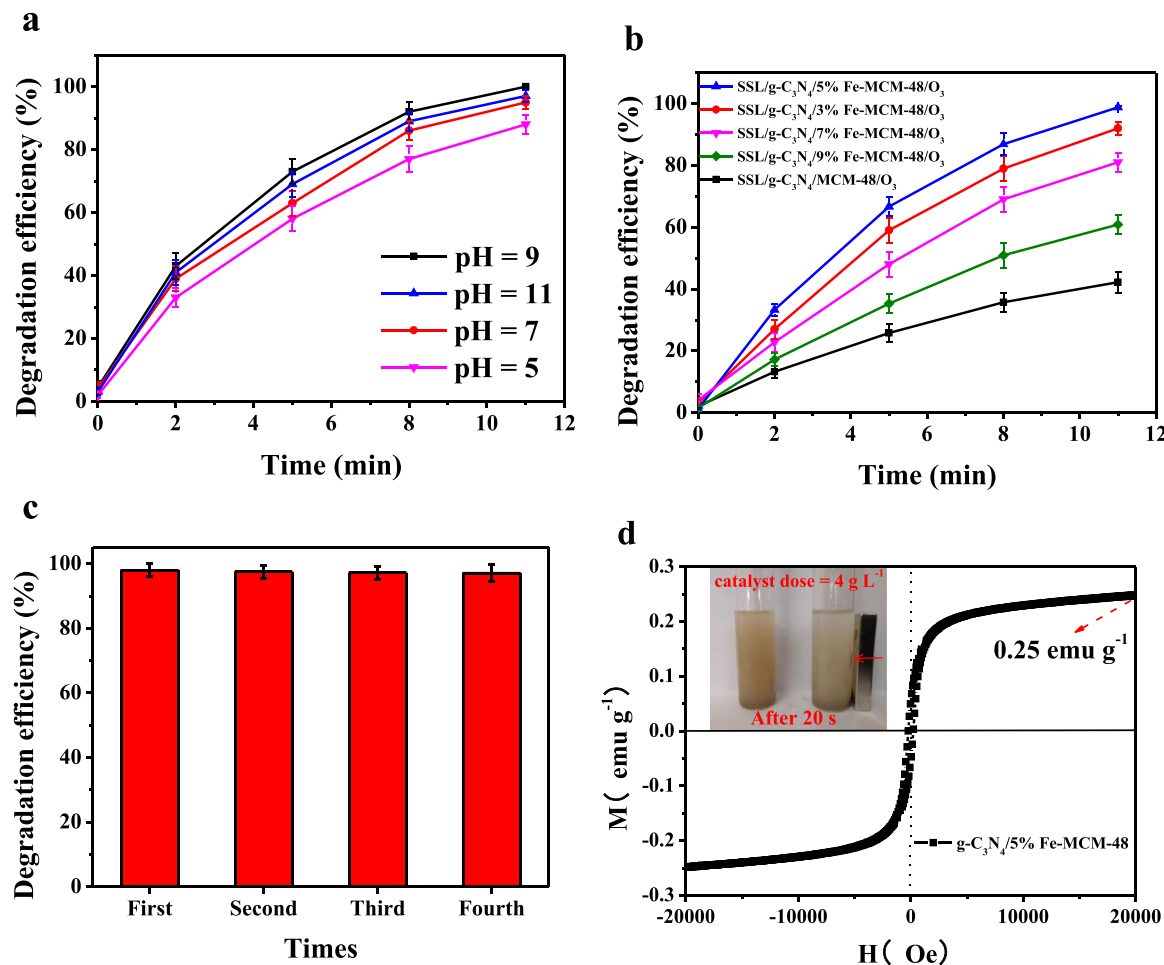


Fig. 7. Influence of initial pH (a) and $\text{Fe}(\text{NO}_3)_3 \cdot 9 \text{ H}_2\text{O}/\text{CTAB}$ mass ratio (b) on the photocatalytic ozonation of AZY, photocatalytic ozonation of AZY by $\text{g-C}_3\text{N}_4/5\%$ Fe-MCM-48 for four cycles (c), M-H hysteresis loop of $\text{g-C}_3\text{N}_4/5\%$ Fe-MCM-48 at room temperature (d). Reaction conditions: O_3 dose = 50 mg L^{-1} , catalyst dose = 0.2 g L^{-1} , initial concentration of AZY = 50 ppm , and temperature = 298 K .

The stability and recycling of catalyst were critical for the practical application of photocatalytic ozonation. Fig. 7c showed that the AZY removal rates did not decrease significantly and remained above 97% after four cycles, meaning that $\text{g-C}_3\text{N}_4/\text{Fe-MCM-48}$ exhibited excellent stability in organic pollutants removal. Its stability was further studied by Atomic Absorption Spectrometer (AA-1800 C, Macy, Shanghai, China) to measure the dissolution of Fe. The results were measured to be 0.004 mg L^{-1} for 90 min and 0.005 mg L^{-1} for 180 min. It proved that the catalyst maintained a stable structure during the catalytic process. Functionalized Fe compounds was usually investigated by Magnetic hysteresis loops. As showed in Fig. 7d, clear relationship between the saturation magnetization and magnetic field strength (Oe) indicated that the magnetic saturation (Ms) value of $\text{g-C}_3\text{N}_4/\text{Fe-MCM-48}$ was about 0.25 emu g^{-1} . Moreover, $\text{g-C}_3\text{N}_4/\text{Fe-MCM-48}$ expressed good magnetic properties at room temperature, which was important for catalyst recycling in practical application.

3.4. Removal pathway of AZY

Fig. 8 displayed possible removal routes of AZY. Main intermediates of AZY removal with $\text{SSL/g-C}_3\text{N}_4/\text{Fe-MCM-48/O}_3$ process were detected by HPLC-MS/MS. The samples taken after 5 min of reaction generated different intermediates. AZY was attacked by $\bullet\text{O}_2/\bullet\text{OH}/\text{h}^+$ mainly at different positions follows bond cleavage (C-N, and C-O), ring opening and hydrolysis [56]. The attack of ROSs on AZY ($m/z = 748$) led to three rings formation of P1 ($m/z = 735.5$) and P2 ($m/z = 735.5$) by concurrent N and O demethylation with abstraction of a hydrogen atom or

one-electron oxidation. Another attack by ROSs led to separation of D-desosamine or L-cladinose ring to form P3 ($m/z = 593$) and P4 ($m/z = 593$), which were further attacked from the same position to get P5 ($m/z = 434.3$). The loss of desosamine ring got dehydration to form P6 ($m/z = 158.2$). The cleavage of C-N bond and loss of the N-methyl-methanamine in P6 would further form P7 ($m/z = 115.1$).

3.5. Catalytic reaction mechanism

The EPR and quenching experiments were employed to investigate the mechanism of photocatalytic ozonation with $\text{g-C}_3\text{N}_4/\text{Fe-MCM-48}$. As depicted in Fig. 9a, no obvious characteristic peak of DMPO- $\bullet\text{OH}$ was observed in the SSL/O_3 while the EPR spectrum of $\text{SSL/g-C}_3\text{N}_4/\text{Fe-MCM-48/O}_3$ depicted apparent signal. It suggested that the presence of $\text{g-C}_3\text{N}_4/\text{Fe-MCM-48}$ enabled the photocatalytic ozonation process to produce rich $\bullet\text{OH}$. In order to further study the removal mechanism of $\text{g-C}_3\text{N}_4/\text{Fe-MCM-48}$ and the role of $\bullet\text{OH}$ and h^+ active ingredients in photocatalytic ozonation process, quenching experiments were carried out by tert butyl alchol (TBA, 5 mM) and triethanolamine (TEOA, 5 mM) as the $\bullet\text{OH}$ and h^+ scavenger, respectively. As depicted in Fig. 9b, the addition of scavengers significantly inhibited the catalytic activity of coupled system, and the removal rate decreased to 39% and 43%, respectively, indicating that both $\bullet\text{OH}$ and h^+ played important role in the photocatalytic ozonation of AZY with $\text{g-C}_3\text{N}_4/\text{Fe-MCM-48}$.

On the basis of the above analyses, an overall mechanism for effective removal of AZY over $\text{SSL/g-C}_3\text{N}_4/\text{Fe-MCM-48/O}_3$ was proposed and showed in Fig. 10. Under SSL irradiation, both photo-induced e^- and h^+

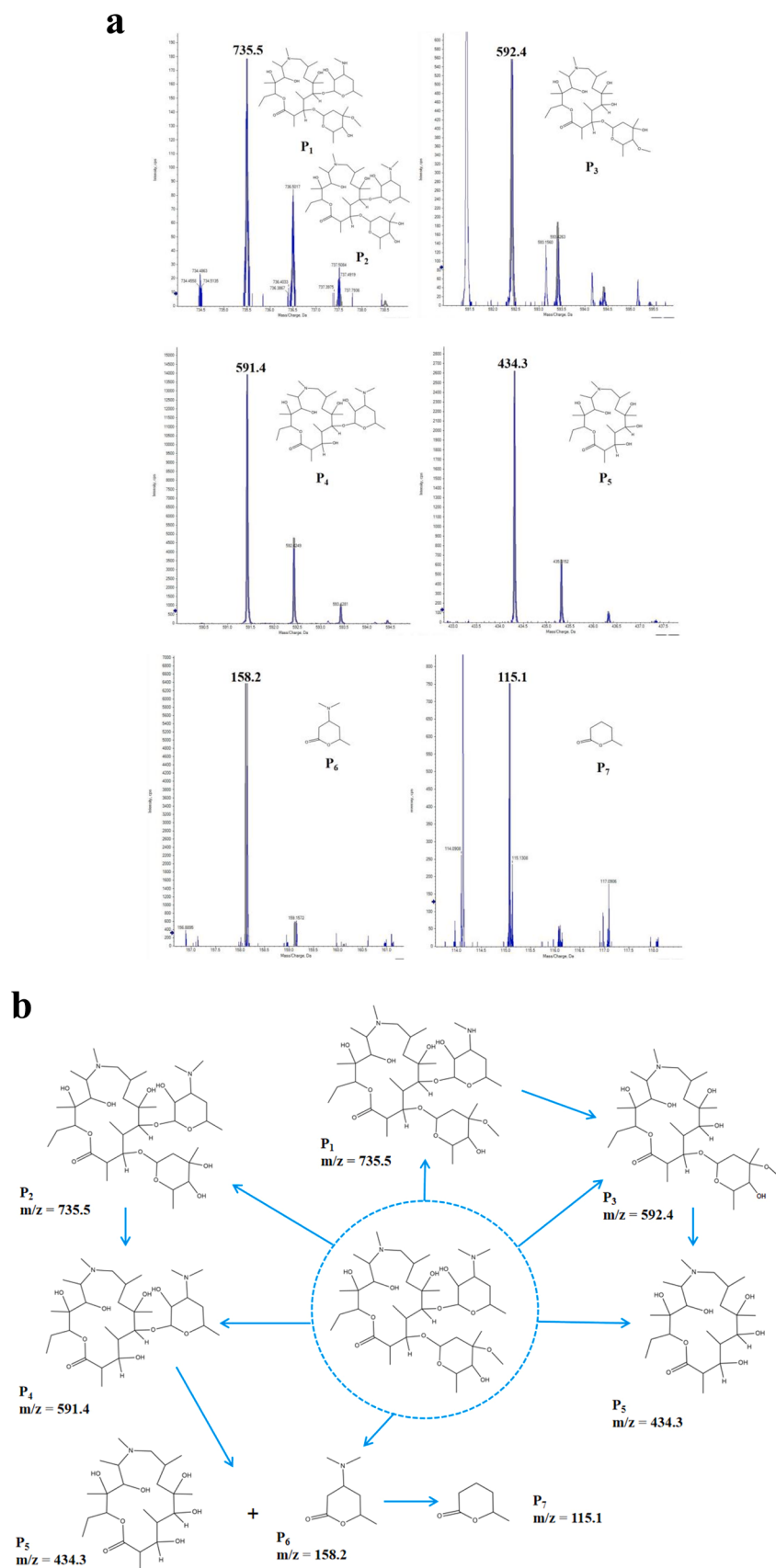


Fig. 8. MS/MS pattern spectra (a) and proposed chemical structures (b) of removal products of AZY.

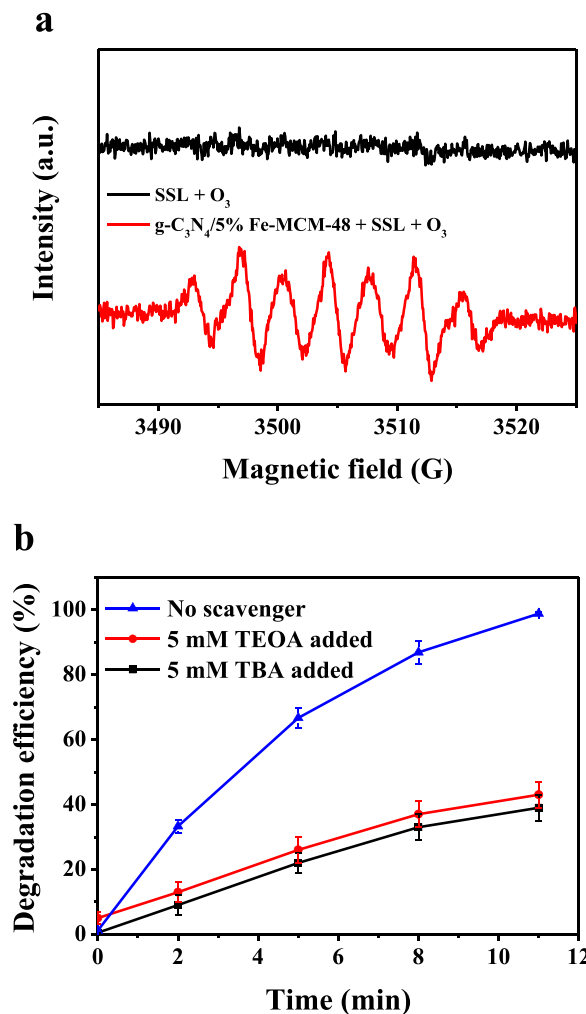
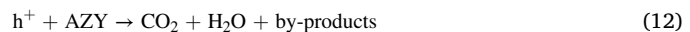
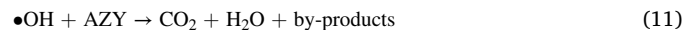


Fig. 9. EPR spectra of DMPO-•OH in the different processes (a) and the AZY removal rate in the presence of different scavengers (b).

were produced after g-C₃N₄ nanosheet was excited (Eq. (7)). The ozonation process mainly involved of directly attacked by O₃ (was generally considered inefficient) and indirectly attacked by ROSSs. Fe acted as active site would accelerate O₃ decomposition to produce large amounts of •OH. The dispersed Fe atoms promoted the transfer of e⁻ and produced •OH by chain reaction with O₃ (Eqs. (8), (9), (10)). Due to the presence of Fe and O₃, effective e⁻ transfer and consumption facilitated the separation of photo-induced carriers and left behind more h⁺. It was well known that both •OH and h⁺ were devoted to the removal of AZY effectively (Eqs. (11), (12)).



4. Conclusion

In this work, the g-C₃N₄/Fe-MCM-48 with unique three-dimension structure was successfully synthesized and its catalytic activity was studied in the photocatalytic ozonation of AZY. The effective AZY removal was achieved by photocatalytic ozonation process with g-C₃N₄/Fe-MCM-48 as catalyst, nearly 100% AZY removal was obtained by SSL/g-C₃N₄/Fe-MCM-48/O₃ after 11 min while it was only 37.3% by SSL/g-C₃N₄/O₃. The significant enhancement mainly corresponded to the fact that Fe atoms of framework were well inlaid three-dimension g-C₃N₄ nanosheet, and they were used as good electron acceptors to enhance the separation of photo-induced carriers and the decomposition of O₃. The increase of specific surface area and the presence of Fe contributed to the efficient synergistic effect between photocatalysis and ozonation. The calculated synergy index was 8.6 for SSL/g-C₃N₄/Fe-MCM-48/O₃. The physics-chemistry properties of g-C₃N₄/Fe-MCM-48 and the reaction mechanism of photocatalytic ozonation were fully discussed in this

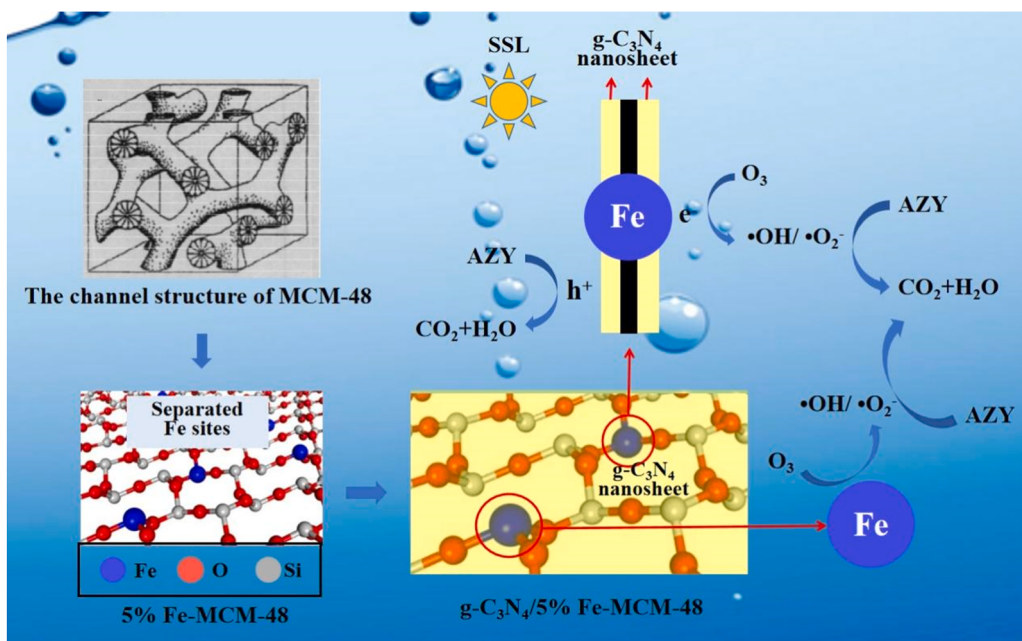


Fig. 10. Proposed photocatalytic ozonation mechanism of g-C₃N₄/5% Fe-MCM-48 for AZY removal.

work. Moreover, g-C₃N₄/Fe-MCM-48 exhibited excellent stability and recycling in the photocatalytic ozonation process and could be used in complex sewage environment. This study given a new view for the sewage treatment of g-C₃N₄-based AOPs.

CRediT authorship contribution statement

Yu Ling: Conceptualization, Methodology, Formal analysis, Investigation, Writing – original draft, Writing – review & editing, **Hai Liu:** Conceptualization, Methodology. **Biqing Li:** Project administration. **Biaojun Zhang:** Conceptualization. **Yixiao Wu:** Conceptualization. **Heping Hu:** Project administration, **Deyou Yu:** Methodology. **Shaobin Huang:** Validation, Supervision, Project administration, Funding acquisition.

Declaration of Competing Interest

The authors declare that they have no known competing financial interests or personal relationships that could have appeared to influence the work reported in this paper.

Data Availability

Data will be made available on request.

Acknowledgements

This work was supported by the Research Project of National Natural Science Foundation of China (No.52270105), the National Key Research and Development Program of China (No. 2019YFC0408605), and the Research Project of China Water Resources Pearl River Planning Surveying & Designing Co. Ltd. (201903).

Appendix A. Supporting information

Supplementary data associated with this article can be found in the online version at [doi:10.1016/j.apcatb.2022.122208](https://doi.org/10.1016/j.apcatb.2022.122208).

References

- [1] Y. Ling, G. Liao, Y. Xie, J. Yin, J. Huang, W. Feng, L. Li, Coupling photocatalysis with ozonation for enhanced degradation of Atenolol by Ag-TiO₂, *Micro-Tube J. Photo Photobiol.* A 329 (2016) 280–286.
- [2] D. Li, J. Huang, R. Li, P. Chen, D. Chen, M. Cai, H. Liu, Y. Feng, W. Lv, G. Liu, Synthesis of a carbon dots modified g-C₃N₄/SnO₂ Z-scheme photocatalyst with superior photocatalytic activity for PPCPs degradation under visible light irradiation, *J. Hazard. Mater.* 401 (2021), 123257 (Article).
- [3] M. Martínez-Polanco, J. Valderrama-Rincón, A. Martínez-Rojas, H. Luna-Wandurraga, M. Díaz-Báez, M. Bustos-López, J. Valderrama-Rincón, Degradation of high concentrations of azithromycin when present in a high organic content wastewater by using a continuously fed laboratory-scale UASB bioreactor, *Chemosphere* 287 (2022), 132191 (Article).
- [4] X. Zhang, H. Zhao, J. Du, Y. Qu, C. Shen, F. Tan, J. Chen, X. Quan, Occurrence, removal, and risk assessment of antibiotics in 12 wastewater treatment plants from Dalian, China, *Environ. Sci. Pollut. Res.* 24 (2017) 16478–16487.
- [5] X. Yi, H. Ji, C. Wang, Y. Li, Y. Li, C. Zhao, A. Wang, H. Fu, P. Wang, X. Zhao, W. Liu, Photocatalysis-activated SR-AOP over PDIH/MIL-88A(Fe) composites for boosted chloroquine phosphate degradation: performance, mechanism, pathway and DFT calculations, *Appl. Catal. B: Environ.* 293 (2021), 120229 (Article).
- [6] G. Ferro, A. Fiorentino, M. Alferez, M. Polo-López, L. Rizzo, P. Fernández-Ibáñez, Urban wastewater disinfection for agricultural reuse: effect of solar driven AOPs in the inactivation of a multidrug resistant *E. coli* strain, *Appl. Catal. B Environ.* 178 (2015) 65–73.
- [7] T. An, H. Yang, G. Li, W. Song, W. Cooper, X. Nie, Kinetics and mechanism of advanced oxidation processes (AOPs) in degradation of ciprofloxacin in water, *Appl. Catal. B Environ.* 94 (2010) 288–294.
- [8] L. Alemany, M. Banares, E. Pardo, F. Martin, M. Galán-Fereres, J. Blasco, Photodegradation of phenol in water using silica-supported titania catalysts, *Appl. Catal. B Environ.* 13 (1997) 289–297.
- [9] Y. Ku, J. Chang, Y. Shen, S. Lin, Decomposition of diazinon in aqueous solution by ozonation, *Water Res.* 32 (1998) 1957–1963.
- [10] Q. Cai, M. Wu, L. Hu, B. Lee, S. Ong, P. Wang, J. Hu, Organics removal and in-situ granule activated carbon regeneration in FBR-Fenton/GAC process for reverse osmosis concentrate treatment, *Water Res.* 183 (2020), 116119 (Article).
- [11] H. Milh, D. Cabooter, R. Dewil, Role of process parameters in the degradation of sulfamethoxazole by heat-activated peroxymonosulfate oxidation: radical identification and elucidation of the degradation mechanism, *Chem. Eng. J.* 422 (2021), 130457 (Article).
- [12] P. Guo, C. Yang, Z. Chu, X. Zhang, G. Sheng, Synchronous reduction-oxidation of 2,4,6-tribromophenol using bifunctional AgPd@CDs in a three dimensional electrochemical reactor, *Appl. Catal. B* 297 (2021), 120467 (Article).
- [13] G. Donoso, J. Dominguez, T. González, S. Correia, E. Cuerda-Correa, Electrochemical and sonochemical advanced oxidation processes applied to tartrazine removal. Influence of operational conditions and aqueous matrix, *Environ. Res.* 202 (2021), 111517 (Article).
- [14] A. Ziyelan, N. Ince, Catalytic ozonation of ibuprofen with ultrasound and Fe-based catalysts, *Catal. Today* 240 (2015) 2–8.
- [15] Y. Wang, Y. Xie, H. Sun, J. Xiao, H. Cao, S. Wang, 2D/2D nano-hybrids of γ-MnO₂ on reduced graphene oxide for catalytic ozonation and coupling peroxymonosulfate activation, *J. Hazard. Mater.* 301 (2016) 56–64.
- [16] A. Safarzadeh-Amiri, O₃/H₂O₂ treatment of methyl-tert-butyl ether (MTBE) in contaminated waters, *Water Res.* 35 (2001) 3706–3714.
- [17] A. Fernandes, M. Gagol, P. Makos, J. Khan, G. Boczkaj, Integrated photocatalytic advanced oxidation system (TiO₂/UV/O₃/H₂O₂) for degradation of volatile organic compounds, *Sep. Purif. Technol.* 224 (2019) 1–14.
- [18] X. Chen, S. Zhan, D. Chen, C. He, S. Tian, Y. Xiong, Grey Fe-CeO_{2- α} for boosting photocatalytic ozonation of refractory pollutants: roles of surface and bulk oxygen vacancies, *Appl. Catal. B* 286 (2021), 119928 (Article).
- [19] M. Mehrjouei, S. Mueller, D. Moeller, A review on photocatalytic ozonation used for the treatment of water and wastewater, *Chem. Eng. J.* 263 (2015) 209–219.
- [20] J. Yang, J. Xiao, H. Cao, Z. Guo, J. Rabeah, A. Brueckner, Y. Xie, The role of ozone and influence of band structure in WO₃ photocatalysis and ozone integrated process for pharmaceutical wastewater treatment, *J. Hazard. Mater.* 360 (2018) 481–489.
- [21] T. Yang, J. Peng, Y. Zheng, X. He, Y. Hou, L. Wu, X. Fu, Enhanced photocatalytic ozonation degradation of organic pollutants by ZnO modified TiO₂ nanocomposites, *Appl. Catal. B* 221 (2018) 223–234.
- [22] A. Rey, P. García-Muñoz, M. Hernández-Alonso, E. Mena, S. García-Rodríguez, F. Beltrán, WO₃-TiO₂ based catalysts for the simulated solar radiation assisted photocatalytic ozonation of emerging contaminants in a municipal wastewater treatment plant effluent, *Appl. Catal. B* 154–155 (2014) 274–284.
- [23] T. Oyama, T. Otsu, Y. Hidano, T. Koike, N. Serpone, H. Hidaka, Enhanced remediation of simulated wastewaters contaminated with 2-chlorophenol and other aquatic pollutants by TiO₂-photoassisted ozonation in a sunlight-driven pilot-plant scale photoreactor, *Sol. Energy* 85 (2011) 938–944.
- [24] X. Huang, J. Yuan, J. Shi, W. Shangguan, Ozone-assisted photocatalytic oxidation of gaseous acetaldehyde on TiO₂/H-ZSM-5 catalysts, *J. Hazard. Mater.* 171 (2009) 827–832.
- [25] G. Liao, D. Zhu, L. Li, B. Lan, Enhanced photocatalytic ozonation of organics by g-C₃N₄ under visible light irradiation, *J. Hazard. Mater.* 280 (2014) 531–535.
- [26] A. Kumar, G. Sharma, A. Kumari, C. Guo, M. Naushad, D. Vo, J. Iqbal, F. Stadler, Construction of dual Z-scheme g-C₃N₄/Bi₄Ti₃O₁₂/Bi₄O₅I₂ heterojunction for visible and solar powered coupled photocatalytic antibiotic degradation and hydrogen production: Boosting via I[–]/I₃[–] and Bi³⁺/Bi⁵⁺ redox mediators, *Appl. Catal. B* 284 (2021), 119808 (Article).
- [27] Q. Liu, Y. Guo, Z. Chen, Z. Zhang, X. Fang, Constructing a novel ternary Fe(III)/graphene/g-C₃N₄ composite photocatalyst with enhanced visible-light driven photocatalytic activity via interfacial charge transfer effect, *Appl. Catal. B* 183 (2016) 231–241.
- [28] Y. Ling, Ga Liao, W. Feng, Y. Liu, L. Li, Excellent performance of ordered Ag-g-C₃N₄/SBA-15 for photocatalytic ozonation of oxalic acid under simulated solar light irradiation, *J. Photo Photobiol.* A 349 (2017) 108–114.
- [29] Y. Qi, C. Guo, X. Xu, B. Gao, Q. Yue, B. Jiang, Z. Qian, C. Wang, Y. Zhang, Co/Fe and Co/Al layered double oxides ozone catalyst for the deep degradation of aniline: preparation, characterization and kinetic model, *Sci. Total. Environ.* 715 (2020), 136982 (Article).
- [30] P. Gan, Z. Zhang, Y. Hu, Y. Li, J. Ye, M. Tong, J. Liang, Insight into the role of Fe in the synergistic effect of persulfate/sulfite and Fe₂O₃@g-C₃N₄ for carbamazepine degradation, *Sci. Total. Environ.* 819 (2022), 152787 (Article).
- [31] S. Li, Y. Tang, W. Chen, Z. Hu, X. Li, L. Li, Heterogeneous catalytic ozonation of clofibric acid using Ce/MCM-48: preparation, reaction mechanism, comparison with Ce/MCM-41, *J. Colloid Interf. Sci.* 504 (2017) 238–246.
- [32] X. Yang, W. Dai, R. Gao, H. Chen, H. Li, Y. Cao, K. Fan, Synthesis, characterization and catalytic application of mesoporous W-MCM-48 for the selective oxidation of cyclopentene to glutaraldehyde, *J. Mol. Catal. A Chem.* (2005) 205–214.
- [33] J. Bing, C. Hu, Y. Nie, M. Yang, J. Qu, Mechanism of catalytic ozonation in Fe₂O₃/Al₂O₃/SBA-15 aqueous suspension for destruction of ibuprofen, *Environ. Sci. Technol.* 49 (2015) 1690–1697.
- [34] S. Li, J. Wang, Y. Ye, Y. Tang, X. Li, F. Gu, L. Li, Composite Si-O-Metal network catalysts with uneven electron distribution: enhanced activity and electron transfer for catalytic ozonation of carbamazepine, *Appl. Catal. B Environ.* 263 (2020), 118311 (Article).
- [35] F. Huang, H. Hao, W. Sheng, X. Dong, X. Lang, Embedding an organic dye into Ti-MCM-48 for direct photocatalytic selective aerobic oxidation of sulfides driven by green light, *Chem. Eng. J.* 432 (2022), 134285 (Article).
- [36] L. Ge, F. Zuo, J. Liu, Q. Ma, C. Wang, D. Sun, L. Bartels, P. Feng, Synthesis and efficient visible light photocatalytic hydrogen evolution of polymeric g-C₃N₄ coupled with CdS quantum dots, *J. Phys. Chem. C* 116 (2012) 13708–13714.

[37] Z. Tong, D. Yang, X. Zhao, J. Shi, F. Ding, X. Zou, Z. Jiang, Bio-inspired synthesis of three-dimensional porous g-C₃N₄@carbon microflowers with enhanced oxygen evolution reactivity, *Chem. Eng. J.* 337 (2018) 312–321.

[38] H. Hassan, M. Betiha, R. Elshaarawy, M. El-Shall, Promotion effect of palladium on Co₃O₄ incorporated within mesoporous MCM-41 silica for CO oxidation, *Appl. Surf. Sci.* 402 (2017) 99–107.

[39] J. Wang, M. Zhang, G. Li, Y. Zhou, Y. Zhang, W. Zhang, T. Jiao, Y. Zhang, P. Liang, H. Zhang, Ultrafine Au nanoparticles confined in three-dimensional mesopores of MCM-48 for efficient and regenerable Hg⁰ removal sorbent in H₂S and H₂O containing natural gas, *Fuel* 286 (2021), 119479 (Article).

[40] N. Sharma, D. Giuliani, K. Kaur, A. Verma, A. Sobe, A. Toor, Enhanced catalytic activity of nano-Fe₂O₃-MCM-48-SO₄ as a green catalyst for the esterification of acetic acid with methanol, *Iran. J. Sci. Technol. Trans. A Sci.* 43 (2019) 2831–2842.

[41] S. Hu, L.W. Yang, Y. Tian, X. Wei, J. Ding, J. Zhong, P. Chu, Simultaneous nanostructure and heterojunction engineering of graphitic carbon nitride via in situ Ag doping for enhanced photoelectrochemical activity, *Appl. Catal. B Environ.* 163 (2015) 611–622.

[42] M. Tahir, C. Cao, F. Butt, F. Idrees, N. Mahmood, Z. Ali, I. Aslam, M. Tanveer, M. Rizwan, T. Mahmood, Tubular graphitic-C₃N₄: a prospective material for energy storage and green photocatalysis, *J. Mater. Chem. A* 1 (2013), 13949 (Article).

[43] Y. Ling, G. Liao, P. Xu, L. Li, Fast mineralization of acetaminophen by highly dispersed Ag-g-C₃N₄ hybrid assisted photocatalytic ozonation, *Sep. Purif. Technol.* 216 (2019) 1–8.

[44] L. Wang, L. Xing, J. Liu, T. Qi, S. Zhang, Y. Ma, P. Ning, Construction of lattice-confined Co-MCM-48 for boosting sulfite oxidation in wet desulfurization, *Chem. Eng. J.* 407 (2021), 127210 (Article).

[45] Y. Yan, X. Wu, H. Zhang, Catalytic wet peroxide oxidation of phenol over Fe₂O₃/MCM-41 in a fixed bed reactor, *Sep. Purif. Technol.* 171 (2016) 52–61.

[46] A. De Stefanis, S. Kaciulis, L. Pandolfi, Preparation and characterization of Fe-MCM-41 catalysts employed in the degradation of plastic materials, *Micropor. Mesopor. Mater.* 99 (2007) 140–148.

[47] X. Li, D. Feng, X. He, D. Qian, B. Nasen, B. Qi, S. Fan, J. Shang, X. Cheng, Z-scheme heterojunction composed of Fe doped g-C₃N₄ and MoS₂ for efficient ciprofloxacin removal in a photo-assisted peroxymonosulfate system, *Sep. Purif. Technol.* 303 (2022), 122219 (Article).

[48] G. Fao, J. Jiang, Theoretical investigation of CO₂ conversion on corrugated g-C₃N₄ surface decorated by single-atom of Fe, Co, and Pd, *Mol. Catal.* 526 (2022), 112402 (Article).

[49] J. Xiao, Y. Xie, F. Nawaz, S. Jin, F. Duan, M. Li, H. Cao, Super synergy between photocatalysis and ozonation using bulk g-C₃N₄ as catalyst: a potential sunlight/O₃/g-C₃N₄ method for efficient water decontamination, *Appl. Catal. B Environ.* 181 (2016) 420–428.

[50] D. Li, C. Wen, J. Huang, J. Zhong, P. Chen, H. Liu, Z. Wang, Y. Liu, W. Lv, G. Liu, High-efficiency ultrathin porous phosphorus-doped graphitic carbon nitride nanosheet photocatalyst for energy production and environmental remediation, *Appl. Catal. B Environ.* 307 (2022), 121099 (Article).

[51] D. Dolat, N. Quici, E. Kusiak-Nejman, A. Morawski, G. Puma, One-step, hydrothermal synthesis of nitrogen, carbon co-doped titanium dioxide (N,C TiO₂) photocatalysts. Effect of alcohol degree and chain length as carbon dopant precursors on photocatalytic activity and catalyst deactivation, *Appl. Catal. B Environ.* 115–116 (2012) 81–89.

[52] I. Grčić, G. Puma, Six-flux absorption-scattering models for photocatalysis underwide-spectrum irradiation sources in annular and flat reactors using catalysts with different optical properties, *Appl. Catal. B Environ.* 211 (2017) 222–234.

[53] R. Acosta-Herazo, M. Mueses, G. Puma, F. Machuca-Martínez, Impact of photocatalyst optical properties on the efficiency of solar photocatalytic reactors rationalized by the concepts of initial rate of photon absorption (IRPA) dimensionless boundary layer of photon absorption and apparent optical thickness, *Chem. Eng. J.* 356 (2019) 839–849.

[54] X. Xu, J. Wang, T. Chen, N. Yang, S. Wang, X. Ding, H. Chen, Deep insight into ROS mediated direct and hydroxylated dichlorination process for efficient photocatalytic sodium pentachlorophenate mineralization, *Appl. Catal. B Environ.* 296 (2021), 120352 (Article).

[55] S. Davoodi, B. Dahrzma, N. Goudarzi, H. Gorji, Adsorptive removal of azithromycin from aqueous solutions using raw and saponin-modified nano diatomite, *Water Sci. Technol.* 80 (2019) 939–949.

[56] A. Kumar, A. Rana, C. Guo, G. Sharma, K. Katubi, F. Alzahrani, M. Naushad, M. Sillanpaa, P. Dhiman, F. Stadler, Acceleration of photo-reduction and oxidation capabilities of Bi₄O₅I₂/SPION@calcium alginate by metallic Ag: wide spectral removal of nitrate and azithromycin, *Chem. Eng. J.* 423 (2021), 130173 (Article).